AVA inversion of the top Utsira Sand reflection at the Sleipner field

Journal:	*Geophysics*
Manuscript ID:	GEO-2010-0301
Manuscript Type:	Technical Paper
Date Submitted by the Author:	15-Sep-2010
Complete List of Authors:	Rabben, Tor; Statoil ASA Ursin, Bjorn; Norwegian Univ of Sci & Tech, Dept of Petr Eng & Appl Geoph
Keywords:	amplitude variation with offset (AVO), inversion
Area of Expertise:	Seismic Inversion

AVA inversion of the top Utsira Sand reflection at the Sleipner field

Tor Erik Rabben[1] **and Bjørn Ursin**[2]

[1]*Statoil Research Centre, Trondheim, Norway, formerly at Norwegian University of Science and Technology, Department of Petroleum Engineering and Applied Geophysics, Trondheim, Norway*

[2]*Norwegian University of Science and Technology, Department of Petroleum Engineering and Applied Geophysics, Trondheim, Norway.*

(June 28, 2010)

Running head:

ABSTRACT

Amplitude versus angle inversion is performed on the top Utsira Sand reflector at the Sleipner field, North Sea, Norway. This interface is of particular interest due to the accumulation of CO_2 injected from a point deeper in the Utsira Sand. The focus is both on the post migration processing of angle gathers together with the actual inversion procedure. The processing treats amplitude extraction, offset-to-angle mapping and global scaling in detail. Two algorithms are used for the inversion, one which assesses uncertainties and one optimized for speed. Both algorithms are very suitable for this type of problem due to their covariance matrices and build-in regularization. In addition two three-parameter approximations of the Zoeppritz equations are used, one linear and one quadratic. The results show significant signals for all three parameters, but a fluid substitution indicates that the contrasts in S-wave impedance and density are overestimated. For the contrasts

in P-wave impedance the results are in agreement with the fluid substitution.

INTRODUCTION

A seismic data set is useful for more than creating a structural image. The seismic amplitudes carry valuable information that, for example, can be inverted for elastic parameters, lithology and fluid content, reservoir parameters or time-laps (4D) changes. In the situation of inversion of elastic parameters the governing model is the Zoeppritz equations. These equations depend on a local reflection and/or transmission angle, and this type of inversion is therefore named amplitude versus angle (AVA) inversion.

Types of AVA inversion differ based on the approximations made to the Zoeppritz equations. If restricted to an isotropic medium and without any approximations it involves five elastic parameters. However, this is very likely to become too ill-posed (Ursin and Tjåland, 1996). Introducing contrasts in elastic parameters, it is possible to do post-stack inversion with only one parameter, P-wave impedance. Another common approximation is the intercept and gradient approach used for cross-plots and AVO classification, this is a two-parameter model valid for small angles and small contrasts. If a third parameter is included, the approximation is valid also for larger angles as long as they are not approaching critical angle (Stovas and Ursin, 2003), but still only for small contrasts. In case of large contrasts it is possible to use the quadratic approximations derived by Stovas and Ursin (2003). These approximations provide increased accuracy without increasing the number of parameters.

In the Sleipner CO_2 injection process (Arts et al., 2008), time-laps seismic is used to monitor the gas injection. Important here is to estimate the total injection volume, in order to map both gas migration paths and how much is dispersed in the brine. Chadwick et al. (2004) show two methods, which at the first glance seem independent, how to estimate injected volumes. One option is to use changes in amplitudes and relate this to thickness of CO_2 using rock physics theory. The second one is to look at time-shifts and convert this into volumes. The problem is that this relation is non-linear, it is therefore necessary to use amplitude information to constrain the time-laps inversion. Therefore, accurate amplitude information is crucial in both methods, and here we present how important it is to use AVA inversion to achieve this. It is usually not stated how the amplitudes are extracted, but Meadows (2008) in his figure 10 shows relative amplitude changes which look very noisy.

In this paper we present both a post-migration workflow and suitable inversion algorithms. We believe that these two are equally important. The workflow emphasizes on amplitude extraction, offset-to-angle conversion and amplitude scaling, all important steps before creating reflection amplitudes proper for AVA inversion. In this process it is necessary to use logs from one well. For the approximation of the Zoeppritz equations we use a three-parameter, isotropic, quadratic model, but we also compare with the linearized version. For the inversion we use two algorithms which both are based on the same Bayesian formulation, one is based on sampling (Rabben et al., 2008) and the other on a least-square formulation (Rabben, 2009). The first one assesses uncertainties, while the second has speed as its advantage. Common for both of them is the ability to impose correlations and spatial coupling via the use of covariance matrices and a built-in automatic, adaptive regularization.

THE SLEIPNER FIELD

Sleipner East and West are two gas and gas condensate fields located in the southern part of the North Sea. Production started in 1993 for Sleipner East and in 1996 for Sleipner West. In the well stream from Sleipner West there is a substantial amount of CO_2 which is separated and injected into the Utsira Sand which is part of the Mio-Pliocene Utsira Formation (Arts et al., 2004). The Utsira Sand is an up to 300m thick sand package extending over 400km in the north-south direction. Sleipner is located in the southern end and the thickness of the sand is 200-300m at a depth of 800m, much shallower than the gas reservoir depth. The Utsira Sand consists of porous, loosely consolidated sandstone (Zweigel et al., 2004). Over the Utsira Sand is a 250m thick package of shales from the Nordland Group, acting as the caprock.

The CO_2 is injected in the lower part of the Utsira Sand, in a 38m long section at a depth of 1010-1013m (Arts et al., 2004). At this position the top of the Utsira Sand has a dome-shaped structure. The injected gas migrates upwards because of buoyancy, all the way to the shale caprock. In 1994, two years before the injection started, the baseline 3D survey was acquired, and repeated 3D surveys were acquired in 1999, 2001, 2002, 2004 and 2006 (Arts et al., 2008). This information is used to track the migration of the injected gas. The post injection surveys show how the Utsira Sand also contains several thin shale layers. The thickness is only a few meters so they are not visible on the 1994 survey. However, they act as barriers for the CO_2 and becomes visible even with only a thin layer of gas, see synthetic modeling in Arts et al. (2004). These shale layers are not fully sealing such that with time the injected gas has migrated all the way to the top of the Utsira Sand.

PREPARATION OF DATA

We will only look at one single survey, the 2001 vintage, and focus only on the top Utsira Sand reflector. This is very similar to the problem Meadows (2008) considered. This reflector is of particular interest because most of the CO_2 will end up here, and the properties of the sand and caprock will determine how the gas migrates. In the spatial domain this will be a 2D problem, where we avoid the estimation of the wavelet. In Figure 1 we see a schematic view of the data processing steps, prior to the inversion, and in the following we will discuss each step in detail.

The input seismic data is time-migrated, but without the NMO correction. A crucial assumption here is that the relative amplitude information is still present, in other words all the preprocessing steps must be amplitude preserving. The fact that the data set is part of a 4D study is an advantage. In Figure 2 we see one single input prestack migrated offset gather from the survey. The spatial position is chosen to be the closest to the well 15/9-13, which we will use later. The top of the Utsira Sand is at about 910ms (this corresponds to 822m) while the base is at 1100ms. For the top Utsira Sand reflection we see good data quality up to source-receiver distance of 1000m. With a simple straight ray approximation we find that this corresponds to a maximum reflection angle $\theta_p = 31°$, see Figure 12 for notation.

The next step in the processing sequence is to extract the amplitude of the top Utsira Sand reflection. The P-wave impedance in the sand is lower than for the shale in the overburden, hence we have to pick the negative maximum (this will be treated more in detail later). The main challenge in this step is to find the NMO-velocities and zero-offset times for the top Utsira Sand reflector. Once we have those we can easily extract the amplitudes from the flattened gathers. We start by applying a constant velocity NMO-correction with $v_{\mathrm{NMO}} = 1900\mathrm{m/s}$, before a near-offset stack. With this image we pick zero-offset times, T_0, for top Utsira Sand. We do this independently for both the inline and crossline direction, compare and use the average in order to avoid wrong interpretations. The final T_0 is shown in Figure 3. The area with inlines larger than 1900 is missing because of difficult interpretation of the reflection due to high noise-level. Next, we generate a densely sampled stacking velocity semblance for a time window around the reflection. With the picked surface information, we are able to have an automated procedure for finding the NMO-velocities for the reflector. We simply choose the velocity corresponding to the maximum semblance value for a small time window around the T_0 pick. Figure 4 shows these stacking velocities for the top Utsira Sand reflector. After the NMO-correction we can extract the minimum amplitude around the T_0 pick, for all spatial points and offsets, to get $a(\bar{x}, \bar{y}, h)$. If we then stack these offsets we get the amplitude map in Figure 5 - a very crude approximation to the zero offset reflectivity. However, it gives a clear impression of the extent of the gas cloud at the top of the Utsira Sand. It is easy to see how it deviates from the background trend. The injection point deep in the formation is located at inline 1840 and crossline 1114.

Our two next steps are simple smoothing and editing. We smooth each offset with a 5×5 Gaussian filter in order to increase the signal-to-noise ratio. However, this has the side effect of smoothing short scale features like the amplitude anomaly extending almost to crossline 1200 in Figure 5. In the same figure we also have a square which indicates the area we are focusing on. It covers inlines between 1712 and 1882, and crosslines between 1005 and 1365 – an area of $8.9\mathrm{km}^2$.

After editing we convert from the offset domain to the angle domain – the angles in the Zoeppritz equations are at reflector depth, not in surface coordinates. For this conversion we assume a 1D velocity profile in the overburden and a constant depth of the reflector. To find this profile we identify key reflectors on a semblance plot, and estimates the interval velocities using Dix' formula. Our final profile is shown in Figure 6. From this we trace rays from the subsurface point and up to the offset, and get an offset-to-angle mapping function that we need.

At this point of the preprocessing, the data set is in the correct domain, but it is only relative amplitudes. In order to get reflection amplitudes $r(x, y, \tilde{\theta})$ we have to scale them properly. Our assumption here is that the scaling is independent of both spatial position and reflection angle, and we end up with the problem of estimating one single scalar factor for the complete data set. A consequence of this is the assumption that the maximum value of the wavelet is constant for all angles. This is supported by the wavelet estimates made by Clochard et al. (2009). To find the scalar we use well log information, that is, P-wave velocity, S-wave velocity and density in both the caprock and the Utsira Sand. With this information we can compute synthetic reflection amplitudes, and compare this with the real data to find the scaling factor. As mentioned before, we have well 15/9-13 available. This is a vertical exploration well with, among others, P-wave velocity, bulk density, caliper and gamma ray available. In Figure 7 we see these four logs in the transition into the Utsira Sand. Immediately we spot the main problem, in the sand the measurements are unreliable. The caliper is hitting its maximum value in the sand zones, most likely because of the very loose sand in the formation. This is also reflected in the velocity and density measurements in these zones. To overcome this we will model the zero offset response and compare with the real data, in order to estimate the acoustic properties.

From the gamma ray we identify four layers: overburden shale, 14m sand (referred to as the sand wedge in parts of the literature), 8m shale (also known as the five-meter shale because of its average thickness in the area) and a sandstone at the bottom. For the shales we have reliable values from the logs, while for the sands we use qualified guesses, both from literature and other logs in the area. These values are also shown in Figure 7. In Figure 8 we see the reflectivity, reflectivity convolved with a wavelet and the real data response. The wavelet we have used is a Ricker wavelet where we have used the data to estimate the peak frequency to be 40Hz. The real data response is a near offset stack. In the figure we see a strong resemblance between the modeled and the real response. We can also see here that main lobe is negative for the top Utsira Sand reflection. However, there will be some side lobe energy from the second shale layer present in our amplitudes.

To map from offset to angle we start by looking at Figure 9, where the amplitudes are plotted against the source-receiver distance, for positions close to the well location. The variation, both between traces and offsets, is large and the data looks very noisy. Using the 1D velocity model we convert from offset to angle domain in Figure 10. When converting we also do a partial angle stack using Gaussian weights in the angle domain. The standard deviation used is 1.5°. The smoothing effect of this is clearly visible, and it looks like (unscaled) reflection amplitudes. Using the Gaussian mean trace we, in Figure 11, compare with synthetic modeling. When generating the synthetic reflection amplitudes we have used the exact Zoeppritz equations, and the P-wave velocity and density from Figure 7. For the S-wave velocities we have used the Mudrock equation (Castagna et al., 1985). We have used this relation also for the shale layer mainly because of the weak dependency between the S-wave velocity and the final scalar value. The anisotropic parameters are from Sollid and Ursin (2003). Firstly, the anisotropic model does not give a good match to our data. Secondly, the difference between the linear and quadratic approximation is very small. However, we are here looking at only one spatial location, in other parts of the data set the difference may be bigger. The amplitudes shown in the figure are now scaled and have become reflection amplitudes. Although it is not a perfect fit with the synthetic modeling, the angle range between 10 and 40 degrees shows a decent match. We will use the partial angle stacks from 16 to 36 with 4 degrees increment, as the input to the inversion.

MODELING AND INVERSION

The forward model we are using is the isotropic, quadratic approximation to PP Zoeppritz equation, derived by Stovas and Ursin (2003),

$$
\begin{aligned}
r_{\mathrm{PP}} = {} & \frac{1}{2\cos^2\theta_p}\frac{\Delta I_\alpha}{\bar{I}_\alpha} - 4\sin^2\theta_s\frac{\Delta I_\beta}{\bar{I}_\beta} - \frac{1}{2}\tan^2\theta_p\left(1-4\gamma^2\cos^2\theta_p\right)\frac{\Delta\rho}{\bar{\rho}} \\
& + \tan\theta_p\tan\theta_s\Bigg[4\gamma^2(1-(1+\gamma^2)\sin^2\theta_p)\left(\frac{\Delta I_\beta}{\bar{I}_\beta}\right)^2 \\
& - 4\gamma^2\left(1-\left(\frac{3}{2}+\gamma^2\right)\sin^2\theta_p\right)\left(\frac{\Delta I_\beta}{\bar{I}_\beta}\frac{\Delta\rho}{\bar{\rho}}\right) \\
& + \left(\gamma^2(1-(2+\gamma^2)\sin^2\theta_p)-\frac{1}{4}\right)\left(\frac{\Delta\rho}{\bar{\rho}}\right)^2\Bigg],
\end{aligned}
\tag{1}
$$

where $\gamma = \bar{\beta}/\bar{\alpha}$ is the background v_S/v_P-ratio, θ_p is the angle of the incoming P-wave (and also the reflected P-wave because of isotropic medium) and θ_s is the angle of the reflected S-wave, see Figure 12. $I_\alpha = \rho\alpha$ is P-wave impedance, $I_\beta = \rho\beta$ is S-wave impedance and ρ is density. ΔI_α is difference between P-wave impedance in the lower and upper media and $\bar{I}_\alpha$ denotes its average, similar definitions for I_β and ρ.

The variable to invert for, the medium parameters, is denoted $\mathbf{m}$ and defined over a two dimensional $n_x \times n_y$ lattice

$$\mathbf{m} = \{m_{ij} \in \mathbb{R}^{D_m}; \quad i = 1..n_y, j = 1..n_x\}, \tag{2}$$

where D_m is the number of medium parameters in each grid cell. With our isotropic approximation we have $D_m = 3$, i.e. $m_{ij} = \{\frac{\Delta I_\alpha}{\bar{I}_\alpha}, \frac{\Delta I_\beta}{\bar{I}_\beta}, \frac{\Delta\rho}{\bar{\rho}}\}_{ij}$. The measurements, $\mathbf{d}$, are defined for the same lattice,

$$\mathbf{d} = \{d_{ij} \in \mathbb{R}^{D_d}; \quad i = 1..n_y, j = 1..n_x\}, \tag{3}$$

where D_d is the number of measured PP reflection amplitudes in each cell. A general requirement is $D_d > D_m$ for the inverse problem not to be underdetermined, and in our case we have $D_d = 6$.

In this notation the forward problem is

$$\mathbf{d} = \mathbf{f}(\mathbf{m}) + \mathbf{e}, \tag{4}$$

with equation 1 as $\mathbf{f}$ and $\mathbf{e}$ a general noise term. To proceed with our Bayesian formulation we assume both the prior of the error and the prior of the medium parameters to be normally distributed, $\pi(\mathbf{e}) = \mathcal{N}(0, \sigma_e^2 \mathbf{S}_e)$ and $\pi(\mathbf{m}) = \mathcal{N}(\boldsymbol{\mu}_m, \sigma_m^2 \mathbf{S}_m)$. Here, $\boldsymbol{\mu}_m$ is the a priori expected value, σ_e^2 and σ_m^2 are scalar variance levels and $\mathbf{S}_e$ and $\mathbf{S}_m$ correlation matrices. The correlation matrices are assumed known while the scalar variance levels are included in the inversion (Buland and Omre, 2003). Because of this we also need prior distributions for the variance levels and we use the inverse gamma distribution, $\pi(\sigma_e^2) = \mathcal{IG}(\alpha_e, \beta_e)$ and $\pi(\sigma_m^2) = \mathcal{IG}(\alpha_m, \beta_m)$. With these two new model parameters, our Bayesian inverse problem now becomes to estimate the joint posterior distribution

$$\pi(\mathbf{m}, \sigma_e^2, \sigma_m^2 | \mathbf{d}) \propto \pi(\mathbf{d} | \mathbf{m}, \sigma_e^2, \sigma_m^2)\, \pi(\mathbf{m}, \sigma_e^2, \sigma_m^2). \tag{5}$$

No analytical solution to equation 5 is known. However, a good approximation is to generate samples from the posterior, in the sense that when the number of samples increases they converge to the posterior. For non-linear likelihoods, this is obtained by the Metropolis–Hastings algorithm (Robert and Casella, 1999; Liu, 2001), and explained in detail by Rabben et al. (2008) for this specific problem. In short, we generate samples from the three full conditional posterior distributions

$$\mathbf{m}^{(i)} \sim \pi(\mathbf{m} | \mathbf{d}, \sigma_e^2, \sigma_m^2), \quad {\sigma_e^2}^{(i)} \sim \pi(\sigma_e^2 | \mathbf{d}, \mathbf{m}), \quad {\sigma_m^2}^{(i)} \sim \pi(\sigma_m^2 | \mathbf{m}) \tag{6}$$

in order to generate a new sample $(\mathbf{m}, \sigma_e^2, \sigma_m^2)^{(i)}$ from the posterior equation 5. Because of convergence properties we do repeated updates of randomly chosen subsets of $\mathbf{m}$ in each iteration $\mathbf{m}^{(i)}$. After generating a sufficient number of samples we are able to inspect the distribution and also calculate statistical properties like mean value and standard deviation.

The sampling approach to approximate the posterior is very convenient since it enables to assess uncertainties, while the drawback is a very computational expensive algorithm. An alternative approximation is to search for only the most likely solution, also known as the maximum a posteriori (MAP) solution or posterior mode,

$$\max_{\mathbf{m}} \pi(\mathbf{m}|\mathbf{d}, \sigma_e^2, \sigma_m^2), \quad \max_{\sigma_e^2} \pi(\sigma_e^2|\mathbf{d}, \mathbf{m}), \quad \max_{\sigma_m^2} \pi(\sigma_m^2|\mathbf{m}). \tag{7}$$

This is an optimization problem, and can be solved by the iterative solution scheme

$$\lambda_{k+1}^2 = \frac{\sigma_{e,k+1}^2}{\sigma_{m,k+1}^2} = \frac{\beta_e + \frac{1}{2}||\Delta\mathbf{d}||_{\mathbf{S}_e^{-1}}^2}{\beta_m + \frac{1}{2}||\Delta\mathbf{m}_\mu||_{\mathbf{S}_m^{-1}}^2} \cdot \frac{1 + \alpha_m + \frac{1}{2}n_m}{1 + \alpha_e + \frac{1}{2}n_e} \tag{8}$$

$$\mathbf{m}_{k+1} = \mathbf{m}_k - \left(\mathbf{J}^T\mathbf{S}_e^{-1}\mathbf{J} + \lambda_{k+1}^2\mathbf{S}_m^{-1}\right)^{-1}\left(\lambda_{k+1}^2\mathbf{S}_m^{-1}\Delta\mathbf{m}_\mu - \mathbf{J}^T\mathbf{S}_e^{-1}\Delta\mathbf{d}\right) \tag{9}$$

where $\Delta\mathbf{d} = \mathbf{d} - \mathbf{f}(\mathbf{m}_k)$, $\Delta\mathbf{m}_\mu = \mathbf{m}_k - \boldsymbol{\mu}_m$, $n_m = n_x n_y D_m$, $n_e = n_m = n_x n_y D_d$ and $\mathbf{J} = \partial\mathbf{f}/\partial\mathbf{m}^T|_{\mathbf{m}_k}$. This algorithm is nothing more complicated than an iterative least-squares inversion with adaptive, data-driven regularization. See Rabben (2009) for a detailed description and derivation of the algorithm.

Before using our inversion algorithm we have to specify some statistical parameters. We start by looking at the two structural covariance matrices, which we define

$$\mathbf{S}_e = \mathbf{g}_e \otimes \mathbf{R}_e \tag{10}$$

$$\mathbf{S}_m = \mathbf{g}_m \otimes \mathbf{R}_m, \tag{11}$$

where '$\otimes$' is the Kronecker product. This assumes that the covariance between any pairs of elastic parameters can be split into a correlation within the two parameters as if they were located in the same spatial point ($\mathbf{g}_e$ and $\mathbf{g}_m$), multiplied by the spatial correlation ($\mathbf{R}_e$ and $\mathbf{R}_m$). The $\mathbf{g}$ matrices have the general form

$$\mathbf{g} = \sigma_i \sigma_j \nu_{ij} \tag{12}$$

with σ_i and σ_j being the standard deviations of medium parameters or noise i and j, and ν_{ij} the correlation between them. For the prior the standard deviation for the contrast in S-wave impedance and density is twice the standard deviation in the contrast in P-wave impedance, while we have no correlations between the three elastic parameters. In matrix notation it is

$$\mathbf{g}_m = \begin{bmatrix} 1.0^2 & 0 & 0 \\ 0 & 2.0^2 & 0 \\ 0 & 0 & 2.0^2 \end{bmatrix}. \tag{13}$$

For the covariances between the noise in the six measurements we have assumed an increase in standard deviation from 1.0 to 2.0 with increasing reflection angle, this due to longer travel time, while again we have no correlations. The latter is supported by looking at Figure 10. Again, in matrix notation this is

$$\mathbf{g}_e = \begin{bmatrix} 1.0^2 & 0 & 0 & 0 & 0 & 0 \\ 0 & 1.0^2 & 0 & 0 & 0 & 0 \\ 0 & 0 & 1.0^2 & 0 & 0 & 0 \\ 0 & 0 & 0 & 1.3^2 & 0 & 0 \\ 0 & 0 & 0 & 0 & 1.7^2 & 0 \\ 0 & 0 & 0 & 0 & 0 & 2.0^2 \end{bmatrix}. \tag{14}$$

For the spatial correlation we are using an exponential correlation function with a constant correlation range r such that the correlation between the two spatial points i and j becomes

$$\mathbf{R} = \exp\left(-3\frac{\delta_{ij}}{r}\right), \tag{15}$$

where δ_{ij} is the distance between points i and j defined on a torus. This torus assumption enables fast matrix inversion by using the fast Fourier transform, see Rue and Held

(2005), but possibly creates some boundary effects. For the medium parameters we have a correlation length $r_m = 100$m and for the noise $r_e = 200$m.

For the a priori expected mean $\boldsymbol{\mu}$ we chose zero contrast for all three elastic parameters. Although this will be far from the truth in the gas zone, it is a safe choice. We will easily see if the posterior solution relies too much on prior information. If not, it is then possible to re-run the inversion using a better prior. In both inversion algorithms we also need an initial $\mathbf{m}_0$, and the natural choice is the expected mean.

In the forward model we need the v_S/v_P-ratio, γ, and the only information we have is from the well location. Therefore, we assume the ratio to be constant for all spatial points, $\gamma = 0.30$. We also need four scalar prior parameters in the two inverse gamma distributions, and following the discussion in Rabben (2009) we choose $\alpha_e = \alpha_m = \beta_e = \beta_m = 0$. Finally, in the Metropolis–Hastings algorithm we are updating $\mathbf{m}^{(i)}$ by repeatedly sampling a subset of $\mathbf{m}$ at a time. In our examples we have used a square of 6×6 spatial points.

RESULTS

We will in this section compare the results from the sampling based inversion algorithm with the MAP estimate. At the same time we will also compare the linear and quadratic forward model.

In Figure 13 we see the expected value and the standard deviation for the sampling based Metropolis–Hasting algorithm, while in Figure 14 we see the same, only with the quadratic forward model as a difference. As indicated in Figure 11, we see that the differences between the linear and non-linear forward models are small. It is only for the S-wave impedance in the area with gas that differences are visible. The lower row displays the standard deviations for the three elastic parameters. There we see that the contrast in P-wave impedance is much less uncertain than the two other, even though we are missing measurements with reflection angles smaller than 16 degrees.

In Figure 15 we have the maximum a posteriori solution for both the linear and quadratic forward models. As for the previous method, the differences between the two forward models are small, and visible only in the injection zone. However, the differences between the two inversion algorithms are substantial for the contrasts in density. In the sampling based result the contrasts are about twice as high compared with the MAP algorithm. As a first reaction this may seem erroneous since the Bayesian model and its parameters are identical for both inversion algorithms. However, both algorithms are depending on convergence in order to sample the joint posterior 5 correctly. We will therefore look at the damping parameter, and we start by looking at the scalar noise and prior variance levels, Figures 16 and 17. The numbers are relative to $\mathbf{S}_e$ and $\mathbf{S}_m$ and thereby not very informative. More interestingly, if we for each sample $^{(i)}$ divide σ_e^2 by σ_m^2, we get samples $\lambda^{2^{(i)}}$. The corresponding distribution is displayed in Figure 18. From the figure we see an expected value of about 0.023, and very similar distributions for the linear and quadratic inversion. The quadratic is the least damped, but the differences are virtually negligible.

For the MAP algorithm we can not assess any distribution of the damping factor, but we can track how it converges. It is convenient to track these changes by looking at the measurement and prior misfit since it will be a direct comparison with the L-curve approach (Lawson and Hanson, 1974; Hansen, 1992) for estimating the damping factor. In Figure 19 we see this for both linear and quadratic inversion. Each red x–mark is an iteration (equations 8 and 9), while the blue line is the L-curve. For the L-curve we see a difference between the linear and quadratic inversion when the λ^2 is small (to the left). This is due to lack of convergence in the matrix inversion in equation 8, and has nothing to do with the inversion method. It will not influence the final solution since it occurs for λ^2 much smaller than our range of interest. In our Bayesian regularization the final damping factors are 0.099 and 0.097 for the linear and quadratic inversion. This is about four times higher than in the sampling based algorithm, which explains the differences we saw previously in this section. However, it is important to note that this differences only appeared for the contrasts in density, which reflects the ill-posedness in three-parameter AVA-inversion.

FLUID SUBSTITUTION

In this section we will perform fluid substitution using Gassmann's equation (Gassmann, 1951) to validate our results by calculating the expected change in contrasts and compare with the inversion results. In all our calculations we will use the MAP inversion result from Figure 15. The first step is to pick a background trend to be our preinjection values of the medium contrasts. The best choice is average values right outside the gas injection zone, and these three values we have used are shown in the first row of Table 1. Of course we acknowledge that we should have used inversion results from the base survey. Particularly for the S-wave impedance and density contrasts there is no clear background trend. Another advantage of using the base survey is to use the repeatability outside the gas zone to quantify the noise level. However, since the scope in this work is the inversion methods, and not time laps effects, we choose to use only a single survey.

Our rock physics parameters are from Arts et al. (2004), and they are summarized in Table 2. With these we first calculate preinjection α_2 and ρ_2 using 0% gas saturation. We also need β_2 and here we use the value from the well-tie. Together with the preinjection contrasts we find the overburden values α_1, β_1 and ρ_1. These three values are unchanged during injection, i.e. no fluid or pressure effects in the overburden.

For the post-injection we begin by performing a fluid substitution, again with the parameters from Table 2. The crucial parameter there is the gas saturation S_g. Chadwick et al. (2004) showed results, from laboratory experiments using core material, how the gas saturation changed with layer thicknesses. For example with a layer thickness of 10m the average gas saturation would be about 0.9. With an assumption of a non-perfect sweep efficiency we use 0.8 in our calculations, but this number is uncertain. With these parameters we first calculate the post-injection values of $\alpha_2, \beta_2, \rho_2$, and then, by using the overburden values, we get the post-injection contrasts in second row of Table 1. To conclude we compare these computed post-injection values with the ones obtained in the inversion. Figure 20 shows a zoom of the area with the gas cloud. For the P-wave impedance we see a very good fit, in the most central areas we have values less than -0.30, although not as low as -0.39. This could be explained with a thinner CO_2 layer or a less efficient sweep. For S-wave impedance the inversion result overestimates the changes. Also for the last parameter, the density, we see an overestimation, but not as severe as for the S-wave impedance. There are several possible reasons for this. It could be due to wrong preinjection contrasts or that the damping factor in the inversion has been too low. Other explanations are the zero prior, the side lobe energy or a wrong v_S/v_P-ratio.

TIME-LAPS APPLICATION

Time-laps seismic is an important tool for monitoring the CO_2 injection. Volume estimates are often extracted and compared with reservoir models and true injected quantities (Chadwick et al., 2004, 2005). As we have demonstrated, amplitudes change dramatically when gas replaces brine, and these changes can be converted to thickness estimates. This procedure can be done shale barrier by shale barrier and the layer thicknesses can again be converted to volumes in order to produce a final volume estimate. Another method for estimating volumes is to use time delays of a key reflector or reflectors relative to the base survey. This can be useful since the propagating seismic waves are very sensitive to the dispersed gas. However, to convert time-shifts into volume estimates an average (trace by trace) gas saturation is needed, and small changes here give large effects in the estimates. The solution is to use amplitude changes to constrain the time-shift inversion (Chadwick et al., 2004). In other words, analysis of amplitude changes is an important tool, and we will therefore look into the details of how to pick amplitudes.

The P-wave velocity is very sensitive to gas saturation, however, for stability purposes it is better to use the P-wave impedance. As we have seen earlier this parameter is well constrained in the inversion. Since twice the P-wave impedance contrast is the zero offset reflection, this quantity can in theory be picked directly from the seismic stack. However, we strongly discourage this simple method. In all seismic experiments it is impossible to have source and receiver located at the same position, and we will therefore never have true zero offset. In our example from Sleipner the smallest offset is 287m, corresponding to a reflection angle of about 12°. Approximations involve either using the smallest offset or a near-offset stack. When picking time-shifts this is appropriate, but not for amplitudes. As long as the reflection amplitudes have a curvature this will either under- or overestimate the amplitude. In our well-tie in Figure 11 the curvature is not very large, but in the gas cloud the curvature is much larger because of a changed density contrasts, and hence the stack approach fails.

CONCLUSION

We have presented how to perform 2D AVA inversion of an interpreted seismic horizon by demonstrating both the workflow for extracting reflection amplitudes and two inversion methods suitable for this problem. In the workflow we have emphasized how to pick and flatten the gathers, conversion from offset to angle and scaling to reflection amplitudes using well log information. The two inversion methods are both based on a Bayesian formulation with flexible covariance matrices. One is a sampling based algorithm able to assess uncertainties, while the other is a fast least-squares variant.

Our application was AVA inversion of the top Utsira Sand reflector at the Sleipner field. Both inversion algorithms experienced nice convergence properties, and resulted in very similar mean and MAP. Only for the contrast in density they differed due to different regularization in the two methods. For the uncertainties we saw a large difference between the parameters. The P-wave impedance had a factor 10 lower standard deviation compared with the S-wave impedance and density contrasts. We also used two different approximations of the PP Zoeppritz equation, one linear and one quadratic. Some differences were found in the gas injection zone, but they were not significant.

By using Gassmann's equation we performed a fluid substitution to calculate post-injection contrasts in the gas injection zone. Although we did not use the 1994 base survey in this work, we showed that the inversion result for the acoustic P-wave impedance is good while the two other contrasts seem to overestimate the effect of the CO_2. We have also shown how this inversion procedure can be very useful to create true zero-offset reflection coefficients. An application is estimation of time-laps amplitude changes.

ACKNOWLEDGMENTS

The results are published with permissions from the CO2ReMoVe project. We wish to thank BP, Schlumberger, Statoil and The Research Council of Norway for their support through the Uncertainty in Reservoir Evaluation (URE) project. We also wish to thank the ROSE project for financial support. Bjørn Ursin has received financial support from Statoil through the VISTA project and from The Research Council of Norway through the ROSE project.

REFERENCES

Arts, R., A. Chadwick, O. Eiken, S. Thibeau, and S. Nooner, 2008, Ten years' experience of monitoring CO_2 injection in the Utsira Sand at Sleipner, offshore Norway: First Break, **26**, 65–72.

Arts, R., O. Eiken, A. Chadwick, P. Zweigel, B. van der Meer, and G. Kirby, 2004, Seismic monitoring at the Sleipner underground CO_2 storage site (North Sea): Geological Society, London, Special Publications, **233**, 181–191.

Buland, A., and H. Omre, 2003, Joint AVO inversion, wavelet estimation and noise-level estimation using a spatially coupled hierarchical Bayesian model: Geophysical Prospecting, **51**, 531–550.

Castagna, J. P., M. L. Batzle, and R. L. Eastwood, 1985, Relationships between compressional-wave and shear-wave velocities in clastic silicate rocks: Geophysics, **50**, 571–581.

Chadwick, R. A., R. Arts, and O. Eiken, 2005, 4D seismic quantification of a growing CO_2 plume at Sleipner North Sea: Petroleum Geology: North-West Europe and Global Perspectives - Proceedings of the 6th Petroleum Geology Conference. Geological Society, 1385–1399.

Chadwick, R. A., R. Arts, O. Eiken, G. A. Kirby, E. Lindeberg, and P. Zweigel, 2004, 4D seismic imaging of an injected CO_2 plume at the Sleipner Field, central North Sea: Geological Society, London, Memoirs, **29**, 311–320.

Clochard, V., N. Delépine, K. Labat, and P. Ricarte, 2009, Post-stack versus pre-stack stratigraphic inversion for CO_2 monitoring purposes: A case study for the saline squifer of the Sleipner field: 79th Annual International Meeting, SEG, Expanded Abstracts.

Gassmann, F., 1951, Über die elastizität poröser medien: Vierteljahrsschrift der Naturforschenden Gesellschaft in Zürich, **96**, 1–23.

Hansen, P. C., 1992, Analysis of discrete ill-posed problems by means of the L-curve: SIAM Review, **34**, 561–580.

Lawson, C. L., and R. J. Hanson, 1974, Solving least squares problems: Prentice-Hall, Englewood Cliffs.

Liu, J. S., 2001, Monte Carlo strategies in scientific computing: Springer.

Meadows, M., 2008, Time-laps seismic modeling and inversion of CO_2 saturation for storage and enhanced oil recovery: The Leading Edge, **27**, 506–516.

Rabben, T. E., 2009, Non-linear Bayesian inversion of seismic reflection amplitudes: PhD thesis, Norwegian University of Science and Technology.

Rabben, T. E., H. Tjelmeland, and B. Ursin, 2008, Non-linear Bayesian joint inversion of seismic reflection coefficients: Geophysical Journal International, **173**, 265–280.

Robert, C. P., and G. Casella, 1999, Monte Carlo statistical methods: Springer.

Rue, H., and L. Held, 2005, Gaussian markov random fields: Chapman & Hall/CRC.

Sollid, A., and B. Ursin, 2003, Scattering-angle migration of ocean-bottom seismic data in weakly anisotropic media: Geophysics, **68**, 641–655.

Stovas, A., and B. Ursin, 2003, Reflection and transmission responses of layered transversely isotropic viscoelastic media: Geophysical Prospecting, **51**, 447–477.

Ursin, B., and E. Tjåland, 1996, The information content of the elastic reflection matrix: Geophysical Journal International, **125**, 214–228.

Zweigel, P., R. Arts, A. E. Lothe, and E. B. G. Lindeberg, 2004, Reservoir geology of the Utsira Formation at the first industrial-scale underground CO_2 storage site (Sleipner area, North Sea): Geological Society, London, Special Publications, **233**, 165–180.

LIST OF FIGURES

Read	$d(z, \tilde{x}, \tilde{y}, h)$
Extract top Utsira Sand	$a(\tilde{x}, \tilde{y}, h)$
Common offset smoothing	$\bar{a}(\tilde{x}, \tilde{y}, h)$
Edit, $x \subseteq \tilde{x}, y \subseteq \tilde{y}$	$\bar{a}(x, y, h)$
Offset to angle mapping	$\bar{a}(x, y, \tilde{\theta})$
Global amplitude scaling	$r(x, y, \tilde{\theta})$
Partial angle stacks, $\theta \subseteq \tilde{\theta}$	$\bar{r}(x, y, \theta)$

Figure 1: Schematic view of our processing steps and corresponding data domain after the operation.

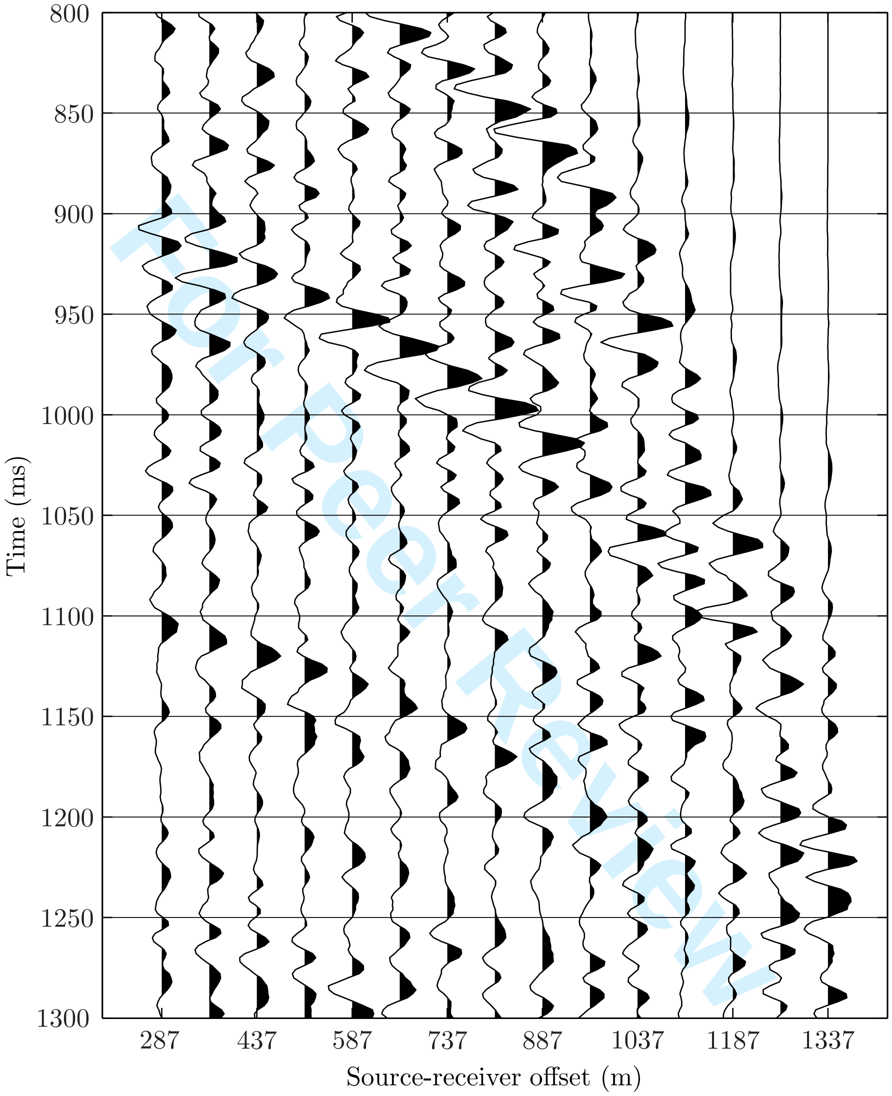

Figure 2: Prestack migrated offset gather from well position. The top Utsira Sand reflector is at 910ms and the base at 1110ms.

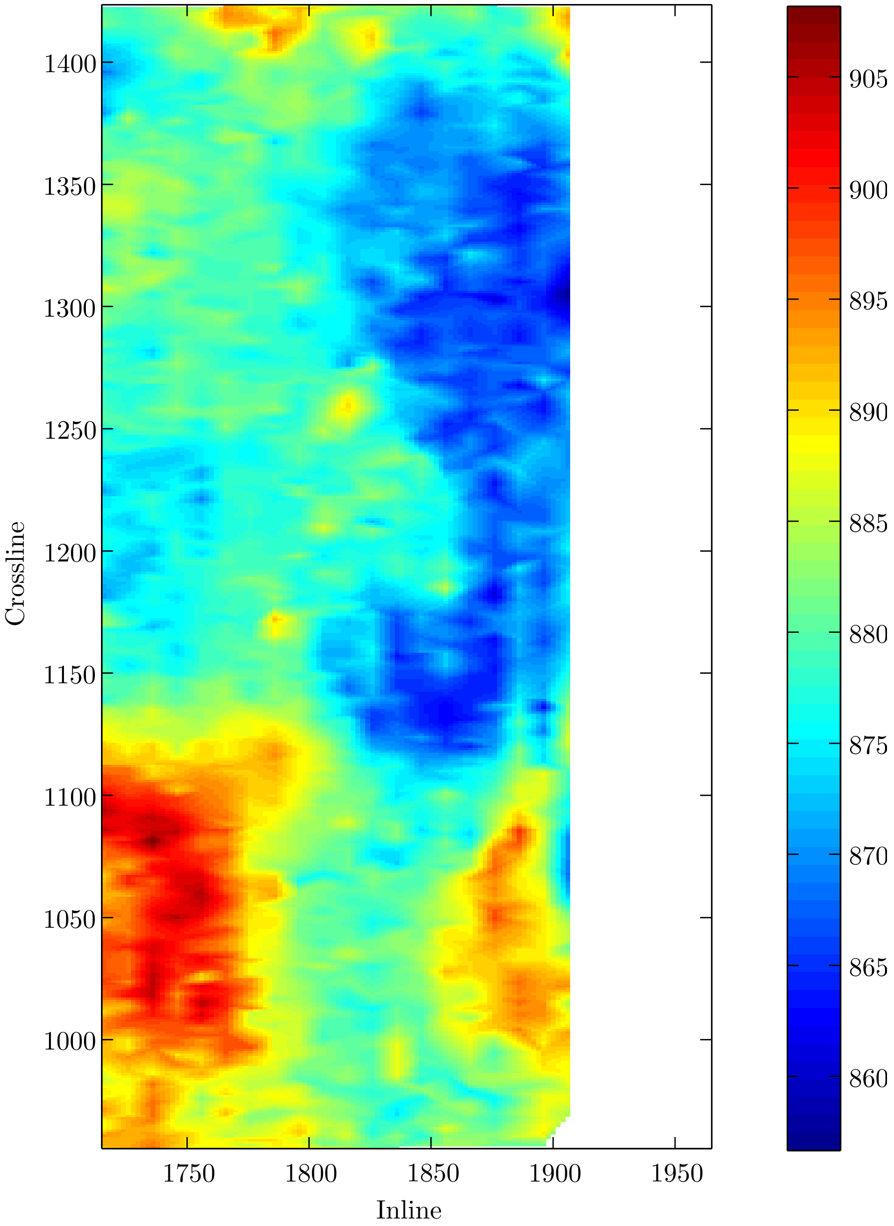

Figure 3: Zero offset two-way travel time, T_0, for the top Utsira Sand reflector.

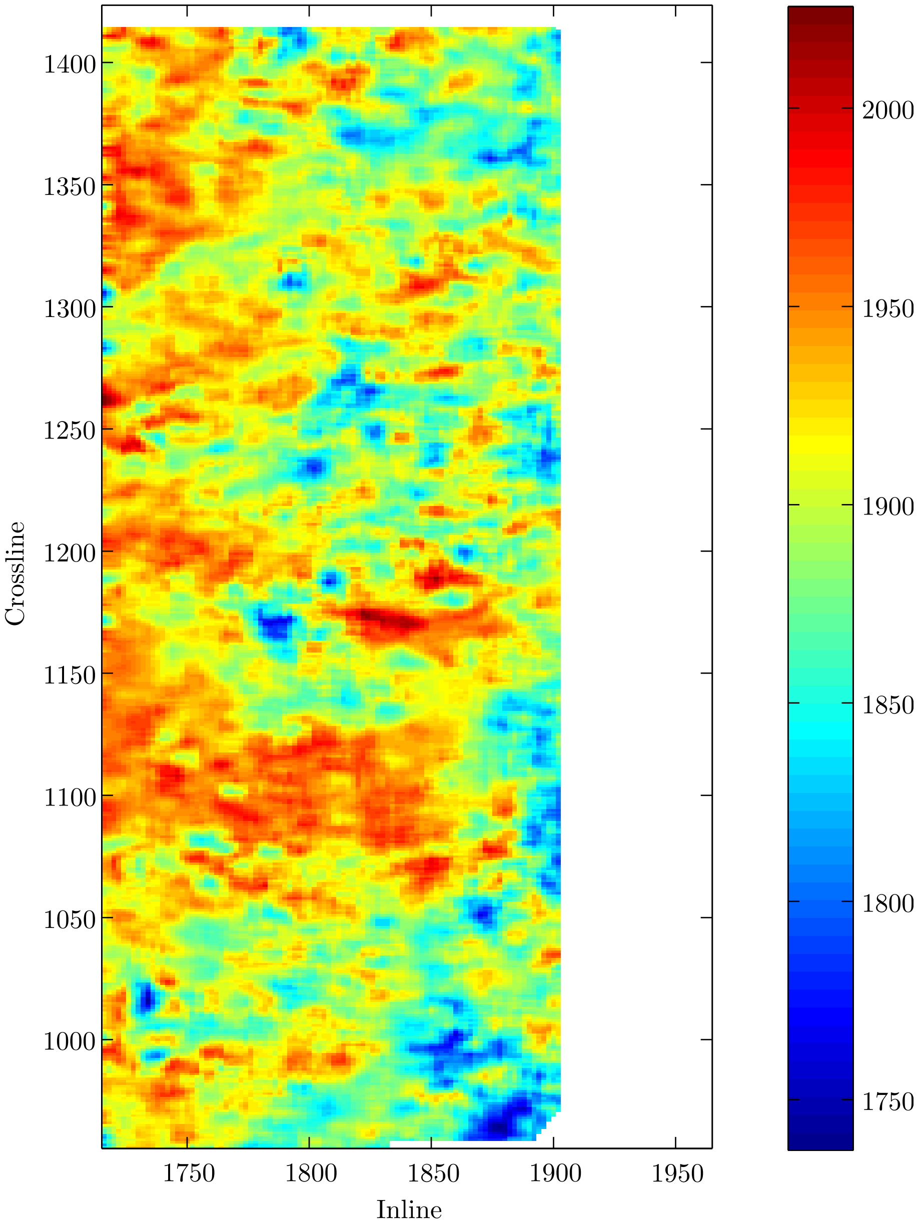

Figure 4: Normal moveout velocity, v_{NMO}, for the top Utsira Sand reflector.

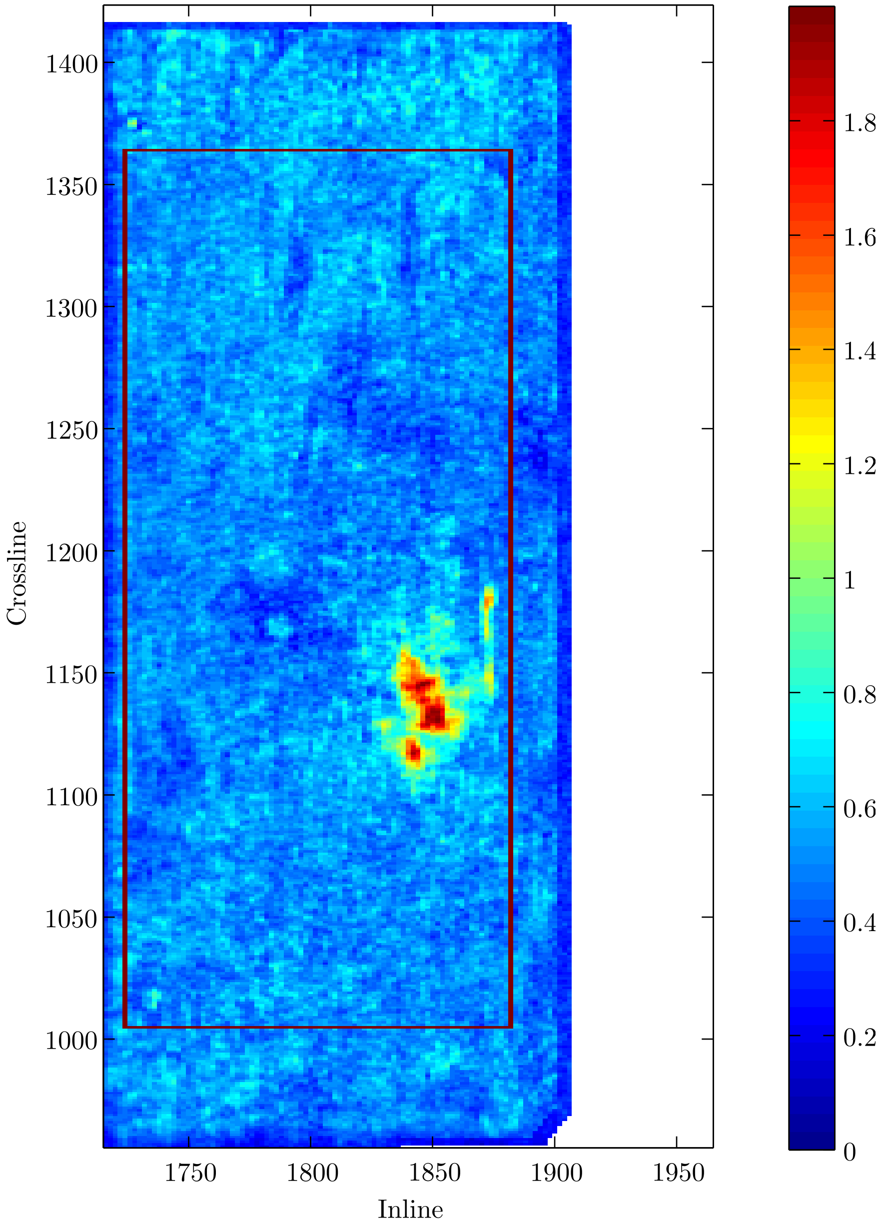

Figure 5: Sum absolute value of the picked amplitudes for the top Utsira Sand reflector. All offsets have been used in the sum.

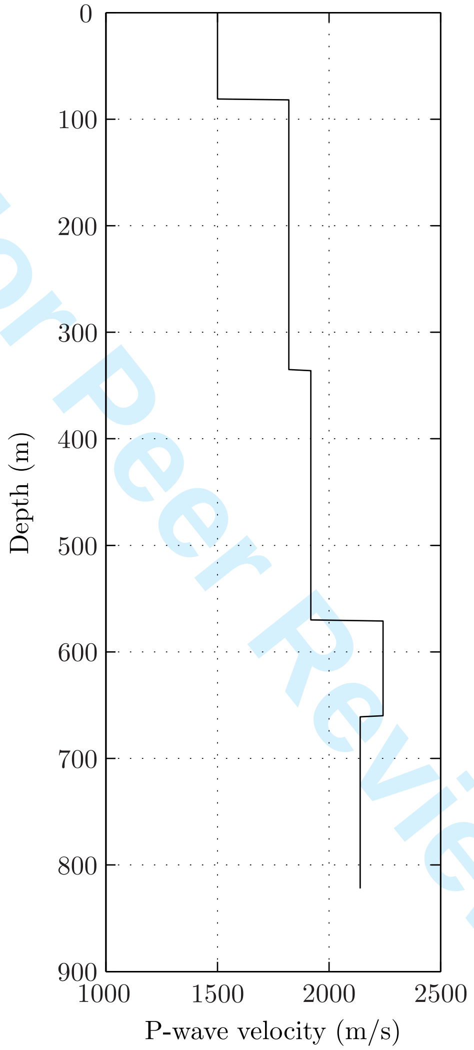

Figure 6: 1D velocity model for overburden.

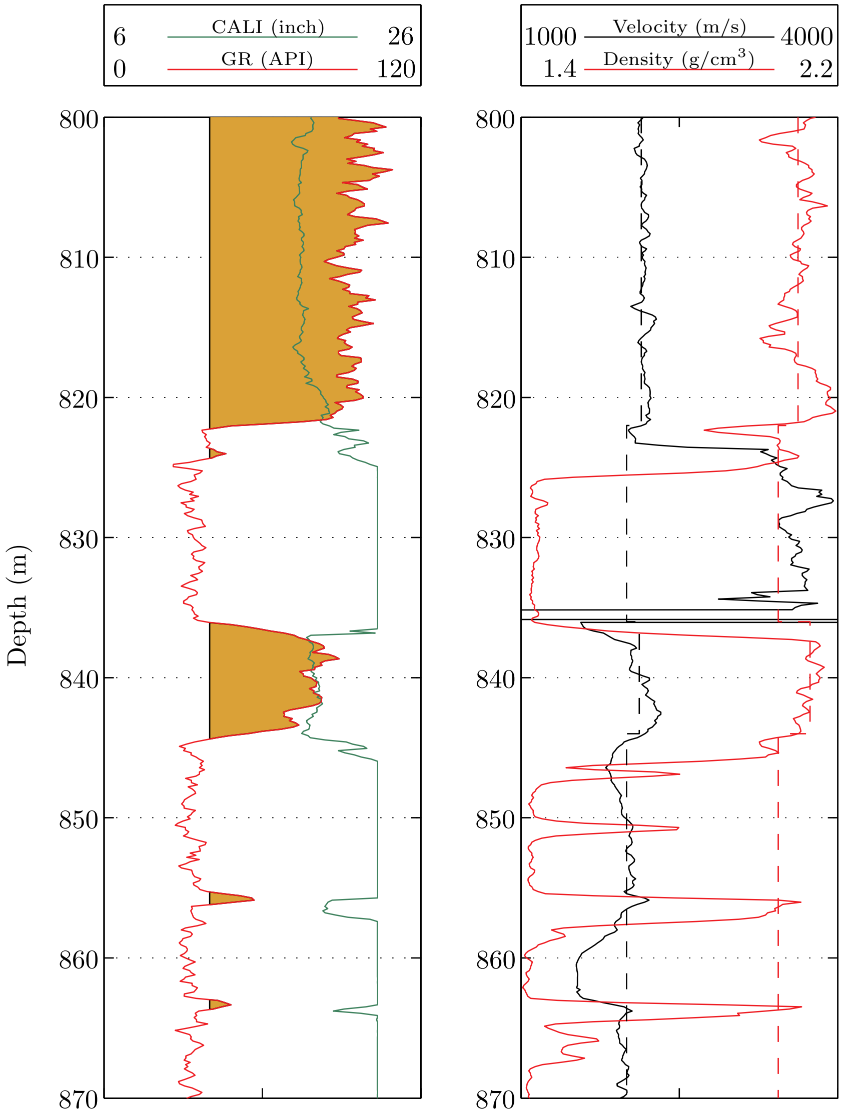

Figure 7: A selection of logs from well 15/9-13. Left we have the caliper log in green and the gamma log in red. Notice how the caliper reaches its maximum where the gamma values are low. To the right we have the P-wave velocity in black and density in red. The continuous lines are log measurements while the dashed are our values used in the synthetic modeling. Again notice how the readings are unreliable where the caliper reaches its maximum.

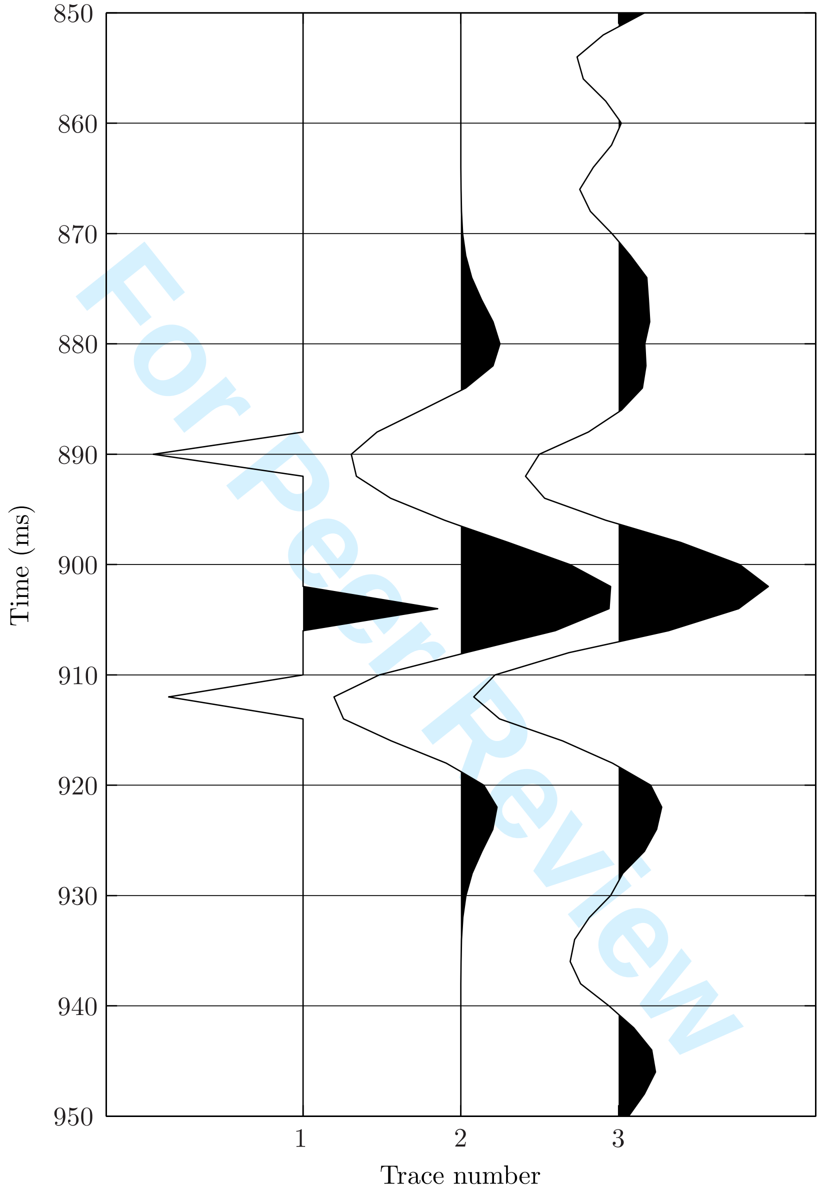

Figure 8: Trace 1 is the synthetic reflectivity, trace 2 is convolved with a Ricker wavelet with peak frequency of 40Hz and trace 3 is a near offset stack of the real data.

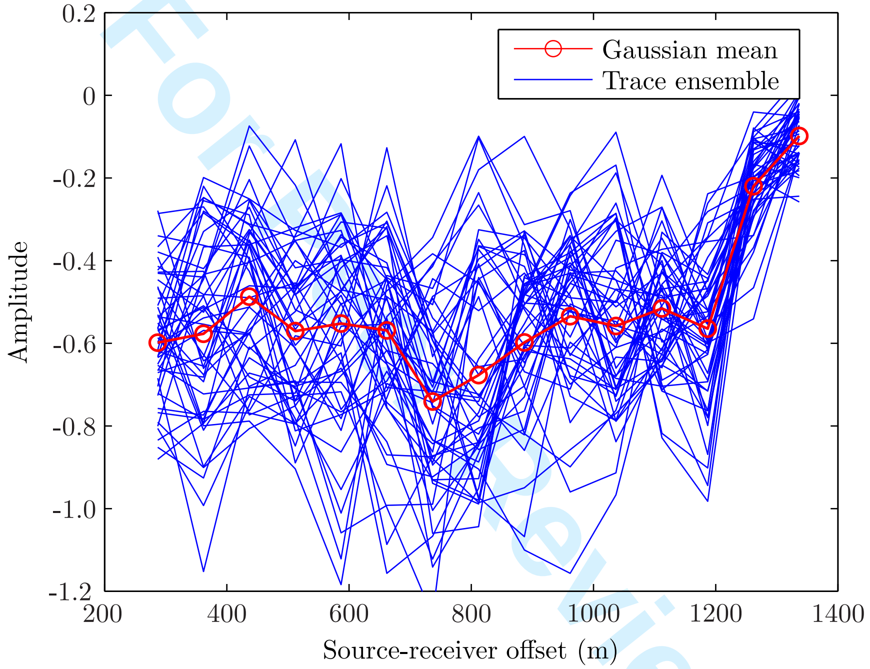

Figure 9: Reflection amplitudes as a function of offset in the vicinity of the well. The red line is the Gaussian mean.

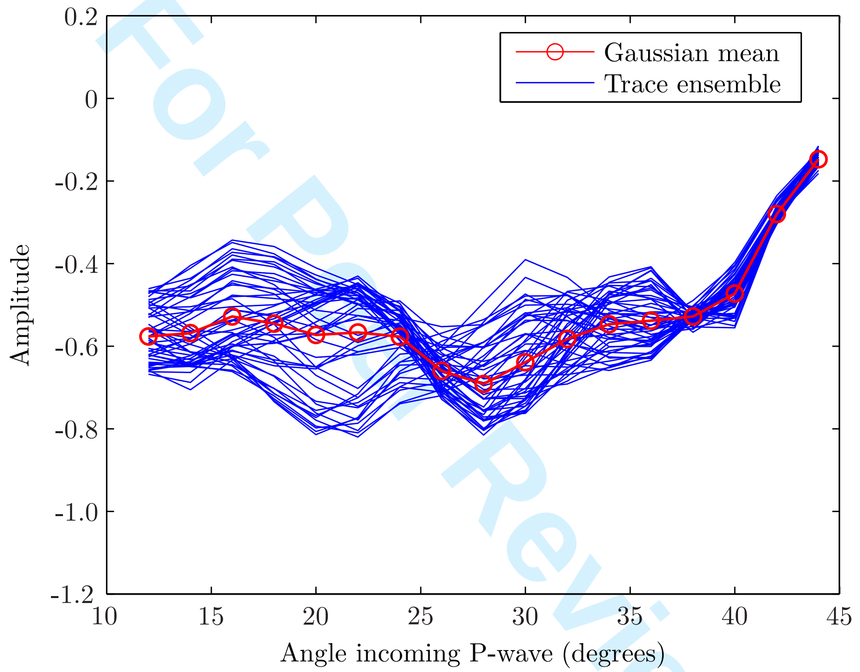

Figure 10: Reflection amplitudes as a function of angle (after the partial angle stack) in the vicinity of the well.

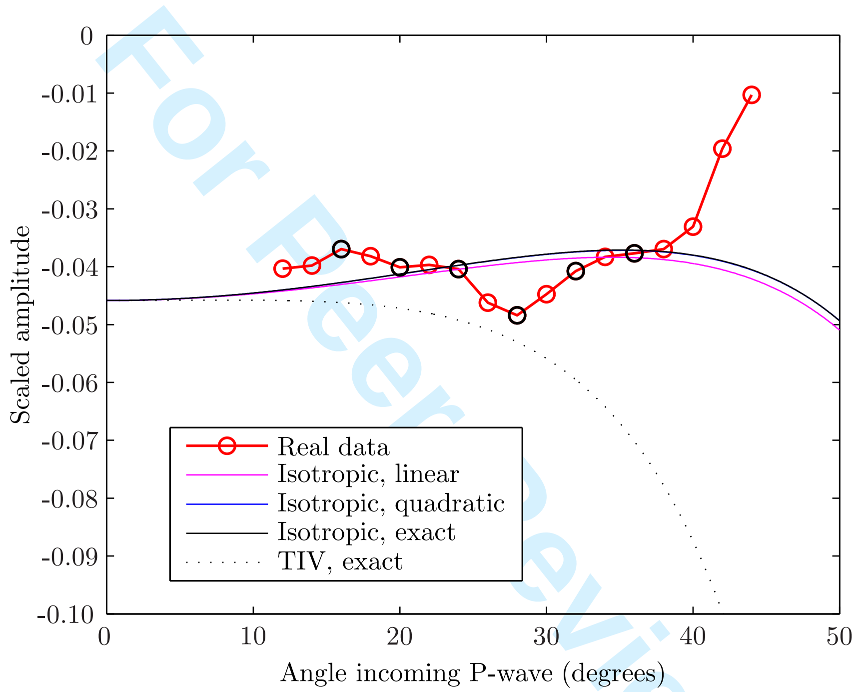

Figure 11: Well-tie between real reflection amplitudes and different forward models using elastic parameters from the well.

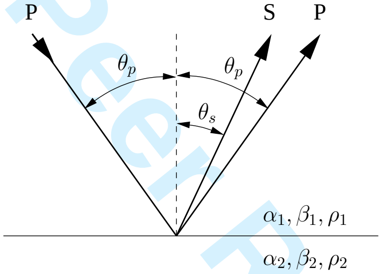

Figure 12: Directions of reflected P and S-waves for an incoming P-wave.

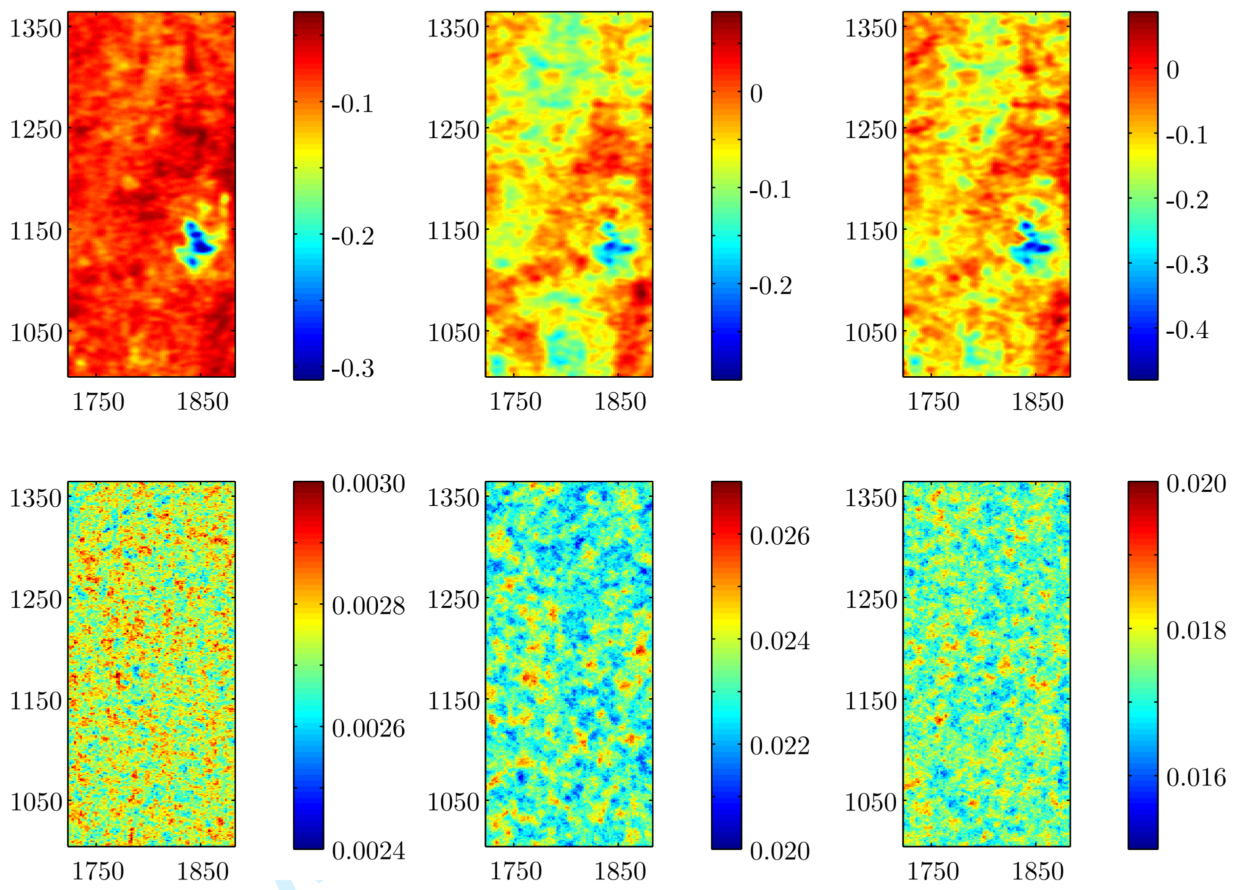

Figure 13: Metropolis–Hastings algorithm using the linear forward model. Expected values (upper row) and standard deviation (lower row) for contrasts in the three elastic parameters P-wave impedance (left column), S-wave impedance (middle column) and density (right column).

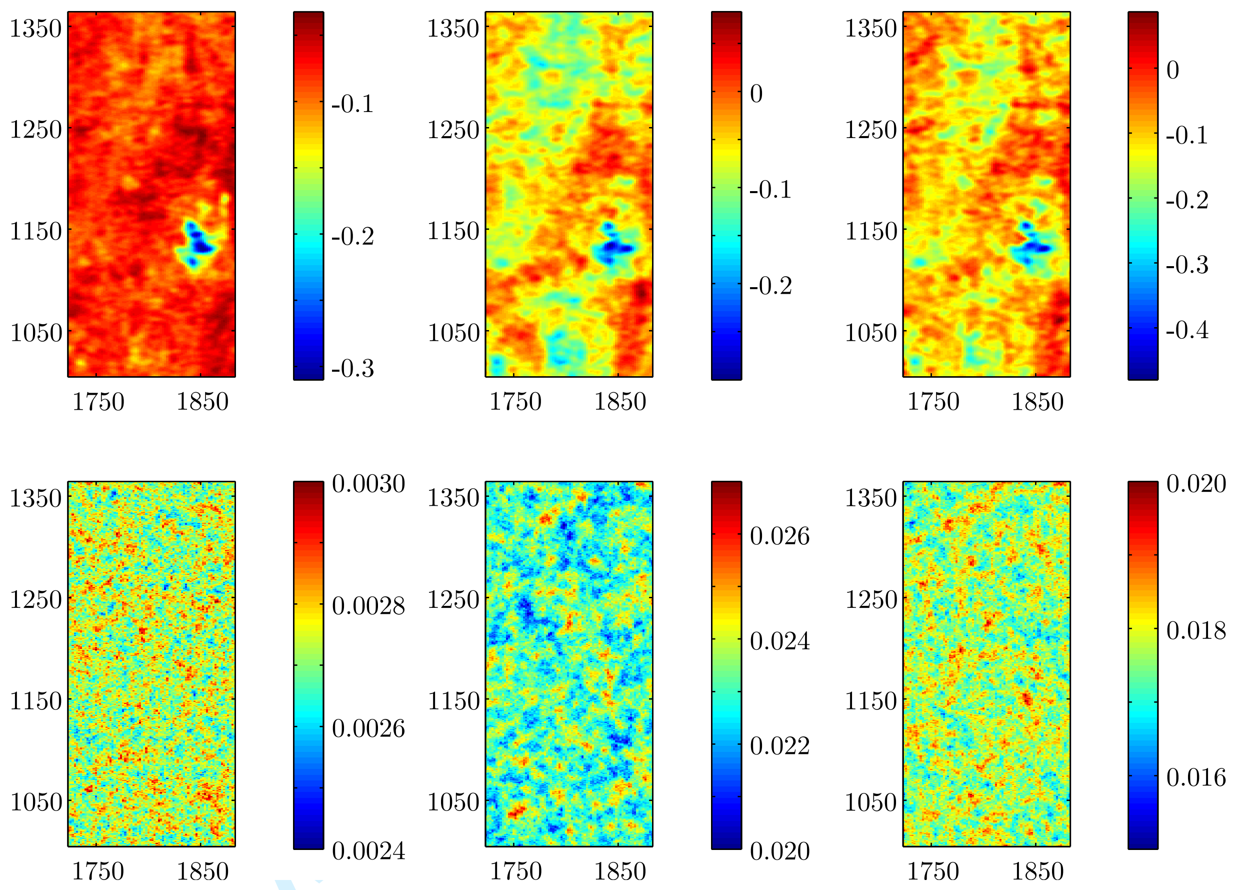

Figure 14: Metropolis–Hastings algorithm using quadratic forward model. Expected values (upper row) and standard deviation (lower row) for contrasts in the three elastic parameters P-wave impedance (left column), S-wave impedance (middle column) and density (right column).

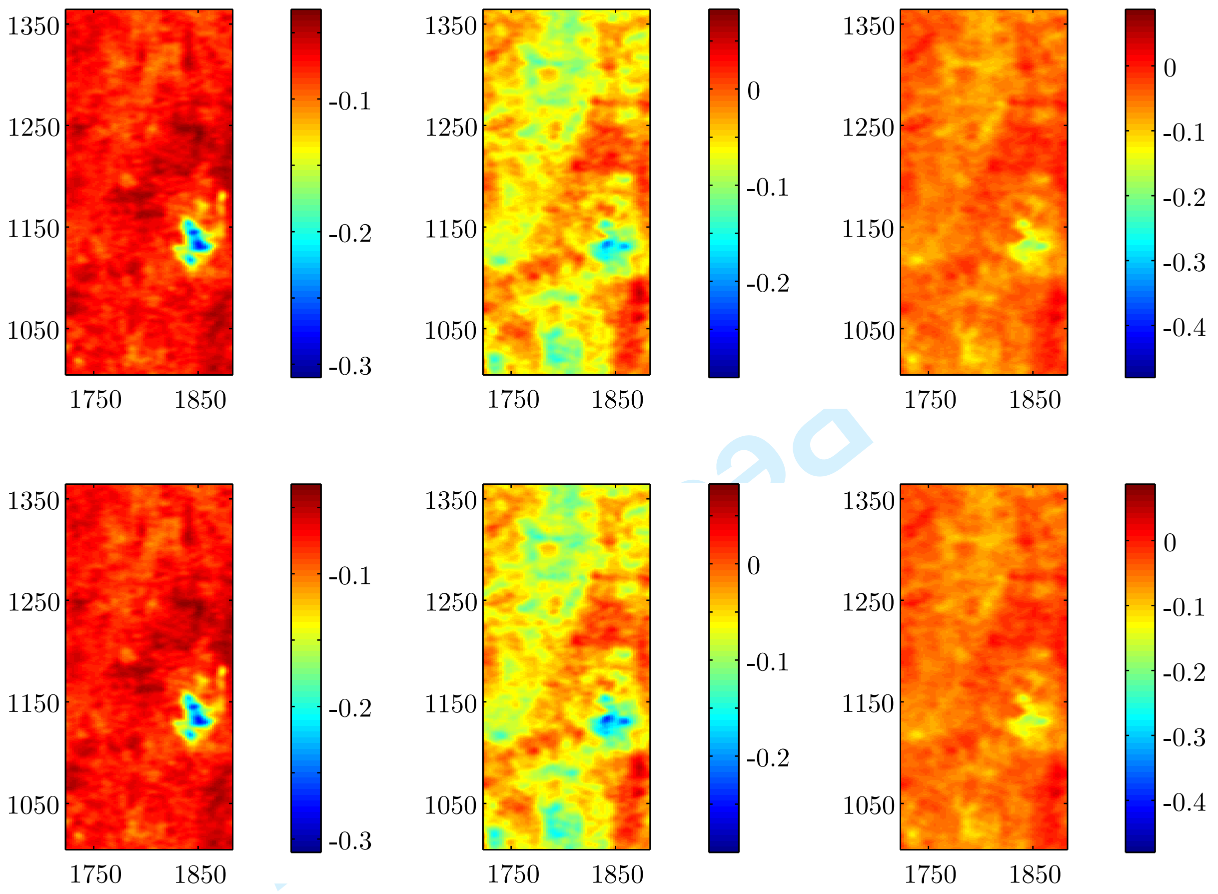

Figure 15: Maximum a posteriori solution with linear (upper row) and quadratic (lower row) forward model for contrasts in the three elastic parameters P-wave impedance (left column), S-wave impedance (middle column) and density (right column).

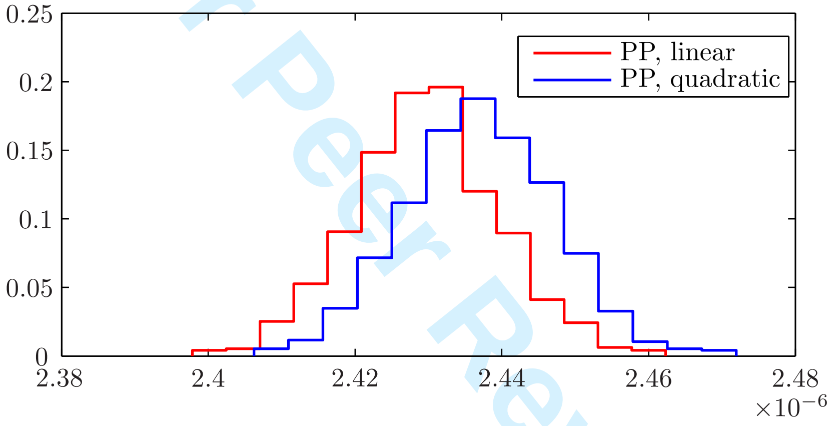

Figure 16: The distribution of the scalar noise variance level σ_e^2.

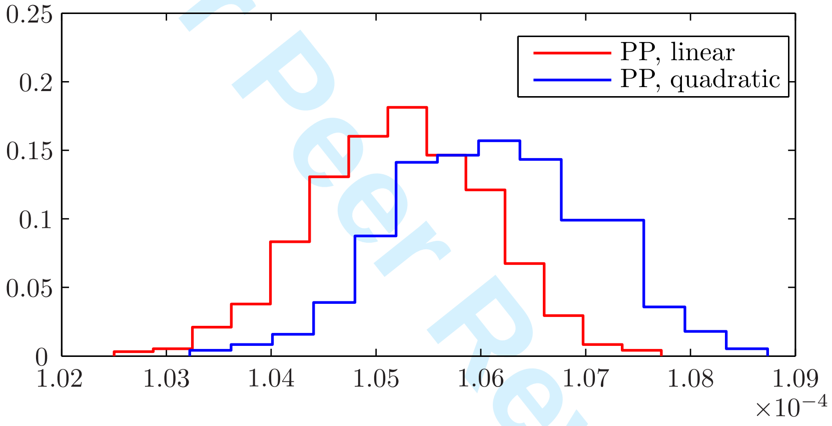

Figure 17: The distribution of the scalar prior variance level σ_m^2.

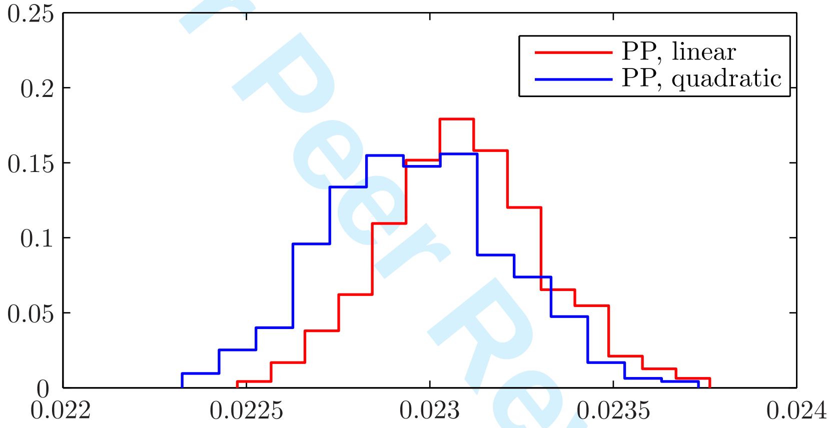

Figure 18: The distribution of the regularization parameter $\lambda^2 = \sigma_e^2/\sigma_m^2$.

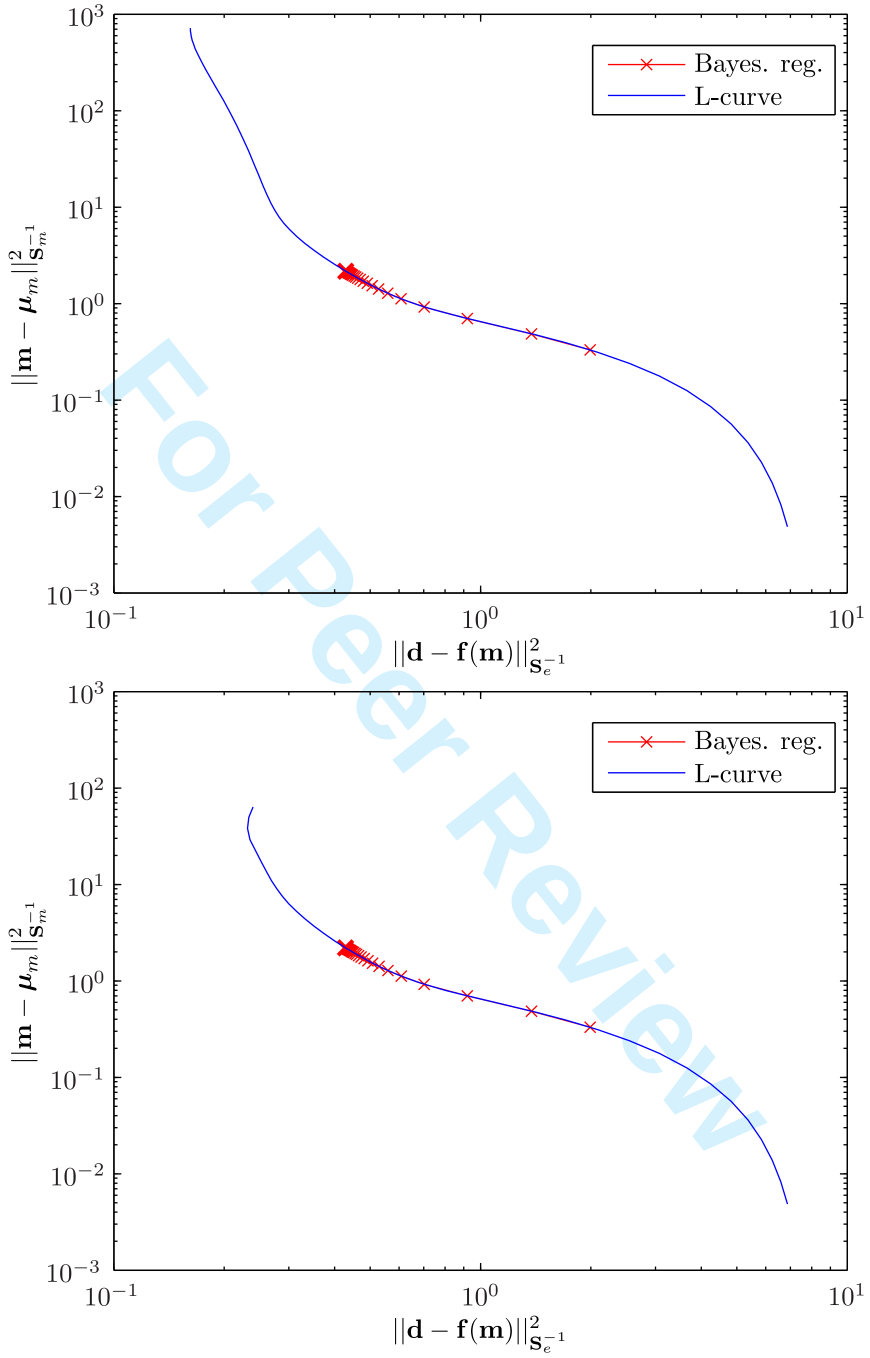

Figure 19: Comparison of the Bayesian regularization and the L-curve approach for the linear (upper) and quadratic (lower) forward model.

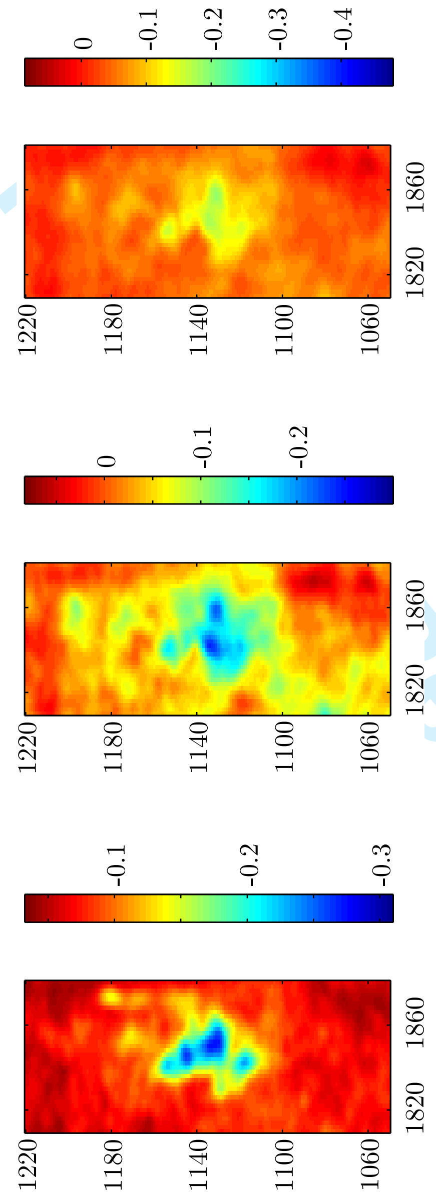

Figure 20: Zoom of the gas cloud in Figure 15. The color scales are kept fixed and therefore do not reflect the minimum or maximum values in the zoomed area.

LIST OF TABLES

Table 1: Contrasts before and after CO_2 injection.

	$\frac{\Delta I_\alpha}{\bar{I_\alpha}}$	$\frac{\Delta I_\beta}{\bar{I_\beta}}$	$\frac{\Delta \rho}{\bar{\rho}}$
Pre injection	-0.07	-0.03	-0.05
Post injection (from Gassmann)	-0.39	-0.05	-0.10
Post injection (from inversion)	-0.28	-0.24	-0.19

Table 2: Rock physics parameters used in Gassmann calculations.

Porosity	37%
Gas saturation	80%
K_{frame}	2.56GPa
K_{sand}	36.9GPa
K_{w}	2.30GPa
K_{CO2}	0.0675GPa
μ	0.85GPa
ρ_{sand}	2650kg/m^3
ρ_{w}	1022kg/m^3
ρ_{CO2}	700kg/m^3